PHYSICAL REVIEW D **87,** 094001 (2013)

Hadronic screening with improved taste symmetry

Sourendu Gupta* and Nikhil Karthik†

Department of Theoretical Physics, Tata Institute of Fundamental Research, Homi Bhabha Road, Mumbai 400005, India

(Received 25 February 2013; published 1 May 2013)

We present our results on meson and nucleon screening masses in finite temperature two flavor QCD using smeared staggered valence quarks and staggered thin-link sea quarks with different lattice spacings and quark masses. We investigate optimization of smearing by observing its effects on the IR and UV components of gluon and quark fields. The application of smearing to screening at finite temperature also provides a transparent window into the mechanism of the interplay of smearing and chiral symmetry. The improved hadronic operators show that for temperature $T \geq 1.5T_c$ (T_c is the finite temperature cross over), screening masses are consistent with weak-coupling predictions. There is also evidence for a rapid opening up of a spectral gap of the Dirac operator immediately above T_c.

DOI: 10.1103/PhysRevD.87.094001 PACS numbers: 12.38.Mh, 11.15.Ha, 12.38.Gc

I. INTRODUCTION

Screening masses control finite volume effects at finite temperature in equilibrium. Studies of the final state of fireballs produced in heavy-ion collisions indicate that they are near equilibrium. Therefore, the study of screening masses a little below the QCD crossover temperature, near the freeze-out, should improve our understanding of experimental conditions. In addition, the vector screening masses below T_c should be of direct relevance to the study of mass spectra of dileptons and photons.

There are also interesting questions about the nature of the high-temperature phase, which are addressed by a study of screening masses. In QCD at temperatures, T, of a few times the crossover temperature, T_c, analysis of the weak-coupling series in powers of the gauge coupling, g, indicates that the physics of the magnetic scale of momentum, g^2T, is potentially nonperturbative. As a result, it may be possible to find phenomena in hot QCD, only involving harder scales, which are amenable to a suitable weak-coupling analysis. For example, the fermionic part of the pressure, as well as its derivatives with respect to chemical potentials, the quark number susceptibilities, seem to admit reasonably accurate weak-coupling descriptions at temperatures of $2T_c$ or above [1].

However, even among static fermionic quantities, screening masses (the inverses of screening lengths) present a confused picture. Most computations have been performed with staggered quarks, and these seem to indicate that there are strong deviations from weak-coupling prediction [2–6]. On the other hand, computations with Wilson quarks give results that are closer to free field theory [7], although they deviate in detail from predictions of weak-coupling theories [8,9]. Since the same pattern is visible in the quenched theory [10], we can attribute the major part of the discrepancy to valence quark artifacts. Here we examine this question systematically using staggered sea quarks and improved staggered valence quarks. Indeed, we see that smeared valence quarks provide a significant improvement. Using these we find that a weak-coupling expansion does work quantitatively for the description of fermionic screening masses at finite temperature. In addition, our results may constrain models of thermal effects on hadrons below and close to the QCD crossover.

A significant technical component of this work is the exploration of the cause of improvement in lattice measurements when smeared gauge fields are introduced into the staggered quark propagators [11–14]. Smeared operators have been explored extensively in the literature earlier [15]. Here we explore optimization of smearing parameters by direct observation of the effects on UV and IR modes separately. It also turns out that the application to finite temperature provides a transparent window into the interplay of improvement and chiral symmetry.

Discussion of technical lattice issues in this paper is confined to the next two sections. Readers who are interested only in the results for thermal physics can read the last two sections.

II. METHODS AND DEFINITIONS

We generated configurations for the Wilson gauge action and two flavors of thin-link staggered sea quarks using the R algorithm. For $am = 0.015$ we used lattice sizes $N_t \times N_s^3$ with $N_t = 4$ and $N_s = 8$, 12, 16, and 24 for finite T studies and scanned a range of gauge couplings, β, to find the crossover coupling β_c. This is completely standard, and the results are collected in the Appendix. The simulations were done using a molecular dynamics (MD) time step $dt = 0.01$ and trajectories with a number of steps, $N_{\rm MD} = 100(N_s/8)$. We checked that halving the time step did not change the results. We observed that it was sufficient to discard the first three hundred trajectories for thermalization. The configurations analyzed were thermally equilibrated and

*sgupta@theory.tifr.res.in
†nikhil@theory.tifr.res.in

spaced one autocorrelation time apart. Details of the runs and statistics are collected in Table I. To set the lattice parameters, we made zero temperature runs at β_c and found $am_\pi = 0.3241(7)$ and $am_\rho = 1.32(9)$. This data set is called the set N in the rest of this paper.

We also studied configurations generated earlier along a line of constant m_π with $N_t = 4$ defined by setting $am = 0.025$ at the corresponding $\beta_c = 5.2875$ [16] and $N_t = 6$ defined by the choice $am = 0.01667$ at its $\beta_c = 5.425$ [17]. The data from Ref. [16] is referred to as set O in this paper, and the data of Ref. [17] is referred to as set P. Hadronic screening masses from the data set P have been reported earlier using thin-link staggered valence quarks [4]; its inclusion in this study enables a clear understanding of the effects of smearing.

We studied screening correlators of mesons and the nucleon. The valence quarks were improved using one-level smeared gauge links [11–14]; the optimization of the smearing algorithm is discussed in Sec. III. In the course of this study, we needed to estimate the extremal eigenvalues of the staggered Dirac operator. This was done using a Lanczos iteration [18]. The tridiagonal matrix generated using this process was diagonalized using the Lapack routine DSTEVX. The investigation of smearing also needed the determination of the taste partners of the pion. For all the correlation functions, we used Coulomb gauge fixed wall sources to project on the modes with vanishing spatial momentum. At $T = 0$ and for temperatures below T_c, multiple wall sources separated by four lattice units were used. We checked that these gave statistically independent results, an observation that could be justified after the fact by the measurement of the Goldstone (local) pion mass.

The screening correlator for the meson γ was parametrized as

$$C_\gamma(z) = A_\gamma \cosh\left[\mu_\gamma\left(\frac{N_s}{2} - z\right)\right] + (-1)^z A'_\gamma \cosh\left[\mu'_\gamma\left(\frac{N_s}{2} - z\right)\right]. \quad (1)$$

The alternating component is absent for the Goldstone pion [19]. Among local operators, we measured the scalar (S) corresponding to the σ/a_0 meson at $T = 0$, the pseudoscalar (PS) corresponding to the π at $T = 0$, the vector (V, ρ at $T = 0$), and the axial vector (AV). At $T = 0$ all three polarizations of the V and AV are equivalent. However, for $T > 0$, we need to distinguish between the spatial (V_s, AV_s) and temporal (V_t, AV_t) polarizations. For the study of taste symmetry, we also measured the nonlocal taste partners in some of these channels. Following Ref. [19], the nucleon correlator is parametrized as

$$C_N(z) = A_N\left\{\exp\left[\mu_N\left(\frac{N_s}{2} - z\right)\right] + (-1)^z \exp\left[-\mu_N\left(\frac{N_s}{2} - z\right)\right]\right\} + A'_N\left\{(-1)^z \exp\left[\mu'_N\left(\frac{N_s}{2} - z\right)\right] + \exp\left[-\mu'_N\left(\frac{N_s}{2} - z\right)\right]\right\}. \quad (2)$$

The screening masses, μ_γ, μ_N, and the remaining parameters were extracted from the measured correlators by fitting to the above forms. The covariance between the measurements at different z were taken care of in the fits. The mean and the error of the parameters were estimated by the bootstrap. Fits were made to the ranges $z_{\min} \le z \le z_{\max}$, where $z_{\max}$ was never more than two sites from the middle of the lattice, $z_{\min}$ was never less than two sites from the source, and the number of data points used was always

TABLE I. The number of independent configurations, N, obtained with the coupling, β, the bare quark mass, am, and the autocorrelation time, τ, for that simulation. Also given are the plaquette value, P, measured at $T = 0$, and the temperature, T/T_c, inferred from it.

	$T = 0$, 16^4			4×16^3			4×24^3		
β	am	P	T/T_c	am	τ	N	am	τ	N
5.25	0.0165	0.4790 (3)	0.92 (1)	0.0165	19	65			
5.26	0.0160	0.4827 (4)	0.96 (1)	0.0160	31	51			
5.27	0.0153	0.4860 (5)	0.98 (1)	0.015	72	48			
5.2746	0.015	0.4873 (4)	1.00						
5.275	0.015	0.4873 (5)	1.01 (1)	0.015	328	76			
5.28	0.0146	0.4887 (6)	1.02 (1)	0.015	65	62			
5.29			1.06 (1)	0.015	21	49			
5.3	0.0138	0.4957 (7)	1.10 (1)	0.0138	8	59			
5.335			1.20 (1)	0.0125	7	75			
5.34	0.0115	0.5100 (2)	1.29 (3)				0.0115	6	50
5.38	0.01	0.5243 (1)	1.51 (5)				0.01	6	57
5.48	0.0075	0.5480 (2)	2.03 (9)				0.0075	3	79

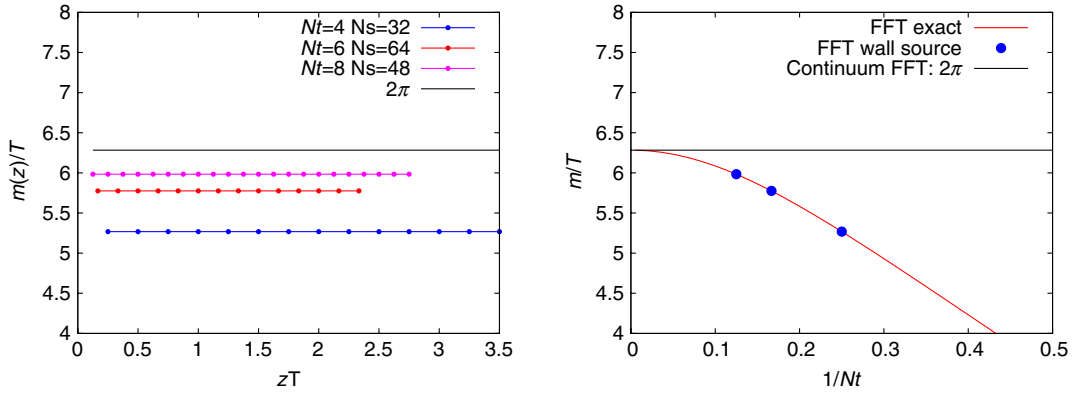

FIG. 1 (color online). Wall sources used on free field theory configurations show no finite volume effects (left) and show controlled finite lattice spacing effects (right).

greater than the number of parameters being fitted. Among the fits satisfying $\chi^2/\mathrm{DOF} < 2$, we chose as the reported estimate of the parameter and its error that which was consistent with the smallest μ within 2σ and had the smallest error. Chiral symmetry restoration can be tested through the mass splittings

$$\Delta_S = \mu_S - \mu_{\mathrm{PS}}, \qquad \Delta_V = \mu_{\mathrm{AV}_s} - \mu_{V_s} \tag{3}$$

as well as the parity projected correlators $C^{\pm S} = C^S \pm (-1)^z C^{\mathrm{PS}}$, $C^{\pm V} = C^V \pm (-1)^z C^{\mathrm{AV}}$ [4].

We computed quantities in a fermionic free field theory (FFT) by numerical inversion of the fermion matrix on a trivial gauge configuration (all links being the unit matrix). These quark propagators were then subjected to exactly the same analysis as in the interacting theory. The negative chiral projections of the screening correlators, $C^{-\gamma}$, vanish in the chirally symmetric phase, and the approach to FFT can be studied using the positive chiral projections, $C^{+\gamma}$. Wall sources work well in FFT, as shown in Fig. 1. Finite volume effects are removed in the projection to the lowest Matsubara frequency, and one can see the expected free field theory behavior in all meson channels for the screening mass: $2\sinh^{-1}\sin(\pi/N_t)$.

III. STUDY OF SMEARING

Smeared gauge links improve the scaling behavior of staggered quarks at finite lattice spacing so that the results approach the unchanged continuum limit faster [15]. This has been measured through staggered pion taste splitting. Optimal parameter values have been obtained numerically, and there have been attempts to understand the results in weak-coupling theories [14].

We examined four schemes that are currently popular: APE [11], HYP [12], Stout [13], and HEX [14]. All these schemes involve replacing the gauge field on a link by a weighted sum of gauge transporters over different paths connecting the end points of this link. The more steps of such smearing we take, the more nonlocal the action becomes. In order to retain a degree of locality compatible with the sea quark action, we restricted ourselves to one step of smearing. The APE and Stout schemes have a single free parameter, ϵ, which determines how much importance is given to link neighbors. The HYP and HEX schemes have three different fattening parameters in three orthogonal directions. We restricted our study to the subset that has equal contributions from all directions, controlled by a single parameter ϵ.

A. Optimization of smearing parameters

The usual lore about smearing is that it suppresses the dependence of operators on high-momentum field modes. Since the lattice cutoff affects UV modes strongly, the result could be closer to the continuum limit. Since field operators have a gauge dependence, it is hard to test this idea directly on gauge fields. Instead, we tested it on the plaquette at a site x averaged over all six orientations, $P(x)$. As for any local operator, one can work with the Fourier transform, $P(k)$, and the power spectrum, $E(k)$, where

$$P(k) = \sum_x \exp(ik \cdot x) P(x) \quad \text{and} \quad E(k) = |P(k)|^2, \tag{4}$$

the mode numbers $k_\mu = \pi(2\ell_\mu + \zeta_\mu)/N_\mu$, N_μ is the size of the lattice in the direction μ, the integers $0 \le \ell_\mu < N_\mu$, and $\zeta_\mu = 0$ for periodic boundary conditions and 1 for antiperiodic. Periodic or antiperiodic boundary conditions imply that the independent modes are those with ℓ_μ inside the Brillouin hypercube in which the body diagonal joins the corners (0,0,0,0) and $(N_x/2, N_y/2, N_z/2, N_t/2)$.

We used this power spectrum to find how smearing affects the UV and IR modes. We separated the IR and UV using hyperplanes perpendicular to the body diagonal. All modes within the Brillouin zone closer to the origin than a hyperplane σ_{IR} were called IR modes; conversely, all modes within the Brillouin zone closer to the far corner than the plane σ_{UV} were called UV modes. Everything else was a generic mode—neither IR nor UV. We defined the suppression of power in the IR and UV as a function of ϵ

$$Q_{\rm UV} = \frac{E_{\rm UV}(\epsilon)}{E_{\rm UV}(0)}, \quad \text{and} \quad Q_{\rm IR} = \frac{E_{\rm IR}(\epsilon)}{E_{\rm IR}(0)}, \tag{5}$$

where $E_{\rm UV}(\epsilon)$ is the power summed over all modes in the UV for a fixed value of ϵ, and $E_{\rm IR}(\epsilon)$ is a similar quantity obtained by summing over all modes in the IR. The definitions of IR and UV are arbitrary, so one needs to check whether the results are sensitive to this definition. We placed the planes $\sigma_{\rm IR}$ and $\sigma_{\rm UV}$ at a fraction d of the length of the diagonal (with $0 < d < 0.5$, so that no mode is simultaneously in the IR and UV) from the nearest corner and varied d. We observed that results were insensitive to d.

We investigated Q numerically with thermalized configurations at $T = 0$ using $\beta = 5.2746$ and $am = 0.015$. Periodic boundary conditions were used so that all $\zeta_\mu = 0$. The variation of Q_X with ϵ is shown in Fig. 2. One sees that the slope of the curve for $Q_{\rm UV}$ always starts off larger than that for $Q_{\rm IR}$. Also, the slope of the latter seems to be close to zero. This shows that smearing can be used to modify the UV without modifying the IR. One can use this to seek an optimum value of ϵ, such that $Q_{\rm UV}$ is as small as possible. In a simulation with dynamical smeared quarks, one would have to do this without making a significant change in $Q_{\rm IR}$. In this study the smearing is quenched; the set of gauge configurations is not changed by smearing, and only valence fermions are affected by smearing. Therefore, in this context we are free to drop the condition on $Q_{\rm IR}$.

We also investigated the quark mass and lattice spacing dependence of $Q_{\rm IR}$ and $Q_{\rm UV}$ by studying thermalized configurations at $T = 0$ using $\beta = 5.2875$ and $am = 0.025$ as well as $\beta = 5.53$ and $am = 0.0125$. The first set has almost the same lattice spacing as the one with $\beta = 5.2746$ but has a somewhat different pion mass. The last two sets have the same pion mass but have lattice spacings that differ by a factor of 2. We show the results in Fig. 2. As can be seen very clearly, there is a change in the overall suppression of power in the IR and UV, but the change in the optimum ϵ is not large even when the lattice spacing is halved. The optimum values of ϵ move down slightly. This movement is compatible with the intuition that finer lattices require less improvement.

Interestingly, conjugate gradient inversion is also optimized at similar values of ϵ [20]. In Fig. 3 we show the number of conjugate gradient (CG) iterations required to invert a smeared staggered Dirac operator, $N_{\rm CG}$, in a representative configuration drawn from thermalized ensembles. These results were obtained with a CG stopping criterion that the norm of the residual is less than $10^{-5}\sqrt{V}$. Note that the performance of the APE and HYP smeared operators are very similar to each other, just as before. The behavior of the Stout and HEX smearing are also similar, but quite different from the previous pair. Again, the lattice spacing and pion mass seems to make little difference to the optimization.

Using the smeared staggered Dirac operator, D, we found the minimum and maximum eigenvalues of $D^\dagger D$: $\lambda_{\rm min}$ and $\lambda_{\rm max}$. We defined the condition number $\kappa(\epsilon) = \lambda_{\rm max}(\epsilon)/\lambda_{\rm min}(\epsilon)$. One expects that the number of CG iterations is closely related to $\kappa(\epsilon)$, as indeed it is seen to be (see Fig. 3). We found that $\lambda_{\rm min}(\epsilon)$ is independent of ϵ to better than 1%, as expected, so $\lambda_{\rm min}(\epsilon)/\lambda_{\rm min}(0)$ is flat. The dependence of κ on ϵ is essentially due to the variation of $\lambda_{\rm max}(\epsilon)$.

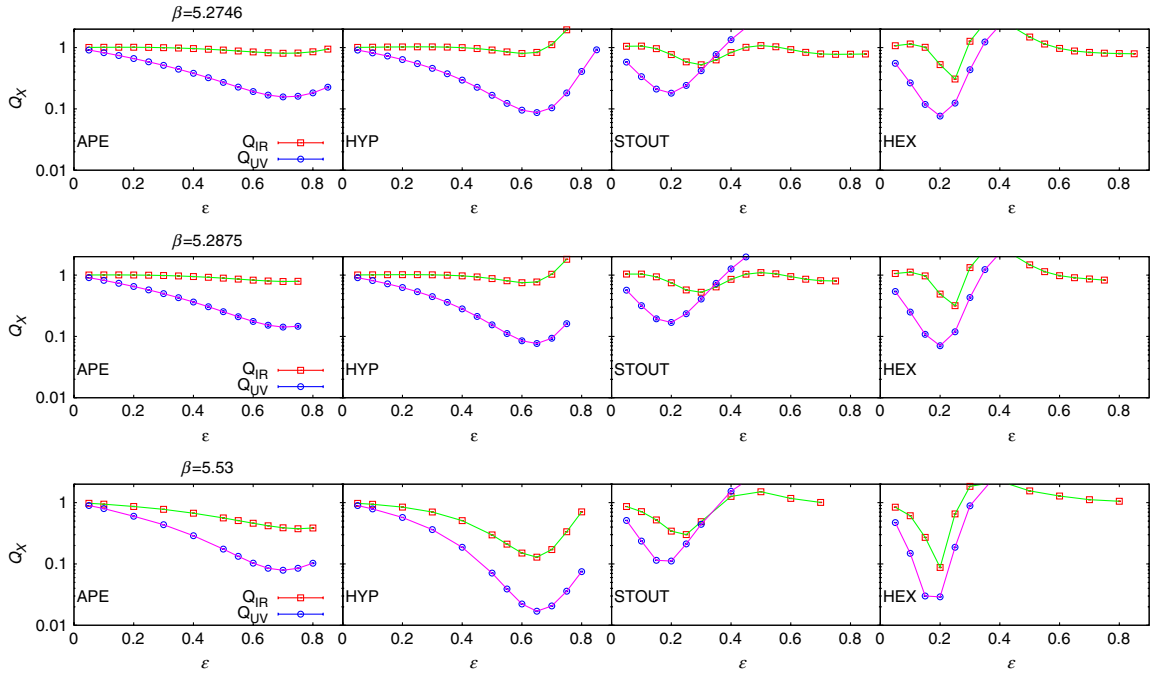

FIG. 2 (color online). Power suppression, Q, in the UV and IR with different kinds of smearing at three different lattice spacings for $T = 0$. A halving of the lattice spacing leads to a weak change in the optimal value of ϵ.

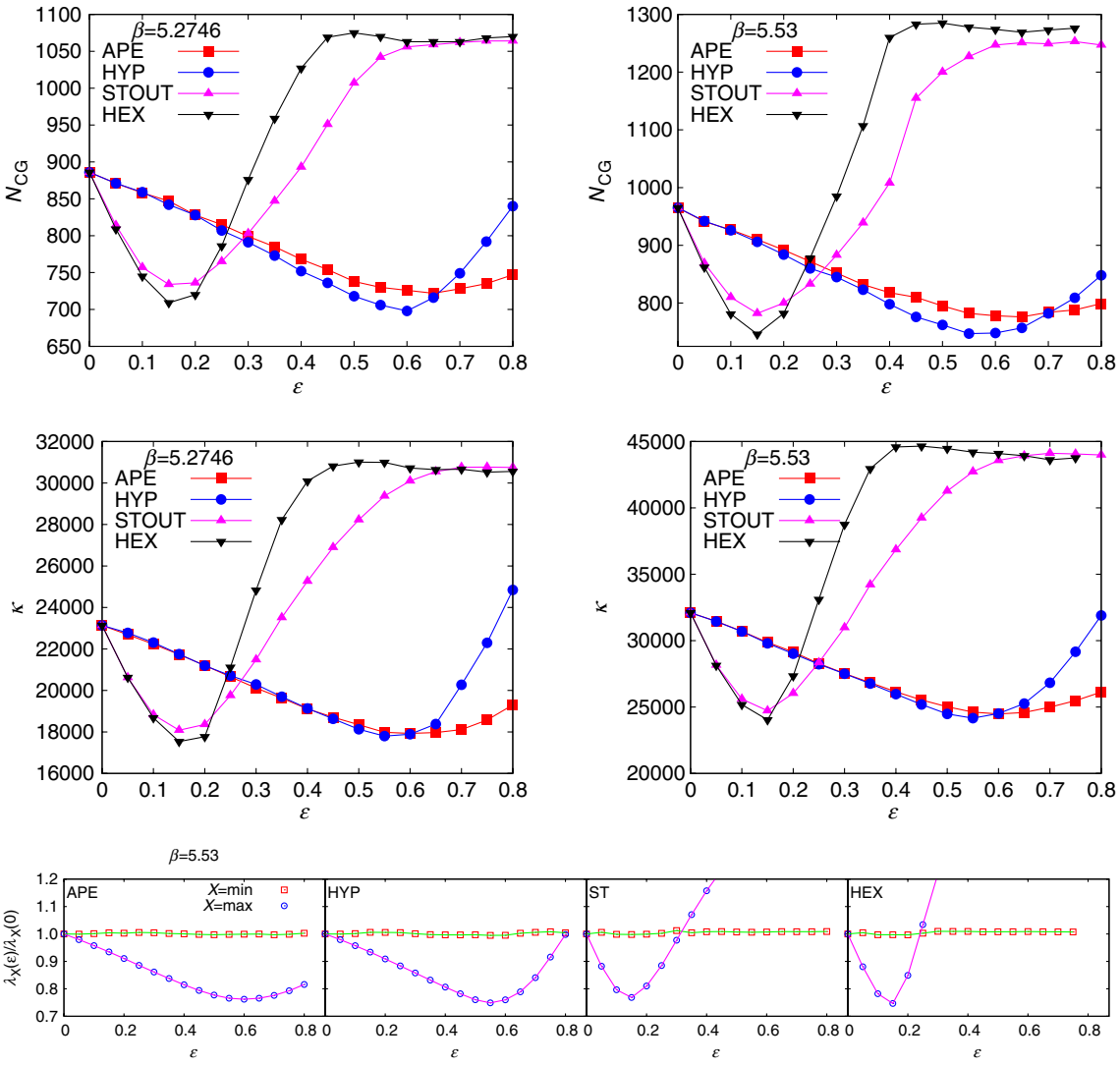

FIG. 3 (color online). Speedup of the conjugate gradient inversion for $T = 0$ at two different lattice spacings as a function of ϵ in the various different smearing schemes. The optimal value of ϵ in each smearing scheme agrees with that seen in the glue sector. This closely follows the change in the condition number, κ, of the fermion matrix. The last panel shows that the change in the condition number comes from the UV, i.e., $\lambda_{\max}$; the IR, i.e., $\lambda_{\min}$, is almost unchanged by smearing.

We can use any of these criteria, namely, the minimization of Q_{UV}, N_{CG}, or $\lambda_{\max}$, to choose the best value of ϵ. The results are shown in Table II in different smearing schemes at different lattice spacings. There is a marginal decrease in the best smearing parameter in each scheme with a decrease in lattice spacing. We see that there is reasonable agreement between the best values obtained through the three methods. Given this, we choose to work with the values $\epsilon = 0.6$ for APE and HYP and with $\epsilon = 0.15$ for HEX and $\epsilon = 0.1$ for Stout.

TABLE II. The best ϵ for two different a, the second being half of the first, evaluated in different schemes and by different optimization criteria. The optimum parameter value in each scheme is nearly independent of a.

	$\beta = 5.2875$, $am = 0.025$			$\beta = 5.53$, $am = 0.0125$		
Scheme	Q_{UV}	N_{CG}	$\lambda_{\max}$	Q_{UV}	N_{CG}	$\lambda_{\max}$
APE	0.71	0.65	0.62	0.70	0.65	0.60
HYP	0.65	0.60	0.56	0.65	0.55	0.55
Stout	0.19	0.15	0.16	0.18	0.15	0.14
HEX	0.20	0.15	0.17	0.17	0.15	0.14

B. Smeared quarks and chirally symmetric correlators

Chiral symmetry restoration in the high-temperature phase of QCD is easily seen in hadronic correlation functions. Below T_c the local meson correlators, S, PS, V, and AV, are quite distinct, but above T_c they collapse into one (see Fig. 4). A pairwise degeneracy of the S/PS and V/AV shows chiral symmetry restoration—and has been demonstrated earlier as well with thin-link staggered valence quarks. However, the near degeneracy of the two pairs at

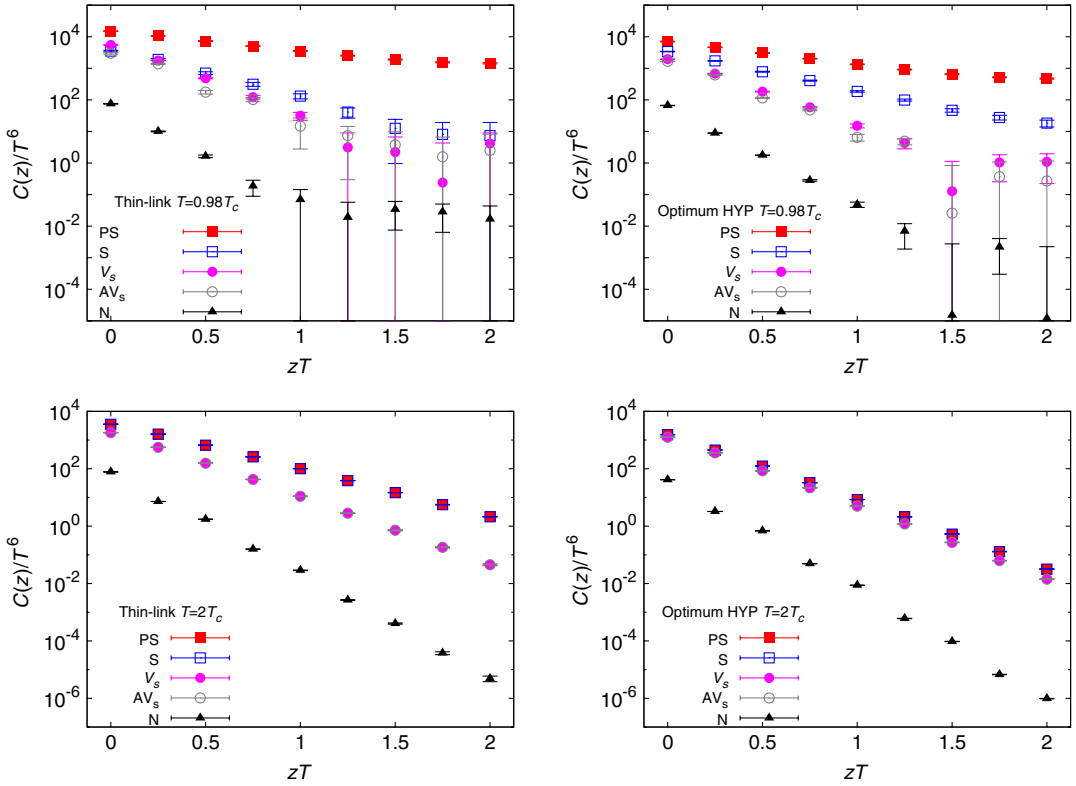

FIG. 4 (color online). Screening correlators from data set N above and below T_c. The signs of chiral symmetry restoration are clear with either thin-link or improved valence quarks in the form of pairwise degeneracies of correlators above T_c. However, improved correlators show even higher degeneracies at high temperature. Similar results are obtained for data sets O and P.

high temperature, visible only after smearing, is a new observation. This occurs in all the data sets: N, O, and P.

Pairwise degeneracy arising from chiral symmetry restoration is most easily seen in the vanishing of $C^{(-S)}$, $C^{(-V_t)}$, and $C^{(-V_s)}$ at high temperature [4]. On examining these combinations, it turns out that the degeneracy for $T > T_c$ becomes clearer with smearing. For example, $C^{(-V_t)}(z = 1/T)$ is $(6 \pm 8) \times 10^{-3}$ at T_c with thin-link valence quarks but becomes $(0 \pm 2) \times 10^{-3}$ when optimal HYP smeared valence quarks are used. The improvement is most remarkable in the S/PS sector, in which we found $C^{(-S)}(z = 1/T) = -3.3 \pm 0.1$ at T_c using thin-link valence but -0.57 ± 0.04 using optimal HYP smeared valence. At larger T all the negative chiral projections vanished. It was seen earlier [4] that $C^{(-V_s)}$ for $T \geq T_c$ vanished when $z > 1/T$ but remained nonzero at short distances. In Fig. 5 we show this effect at T_c and also that it vanishes at $2T_c$. A more detailed view of the

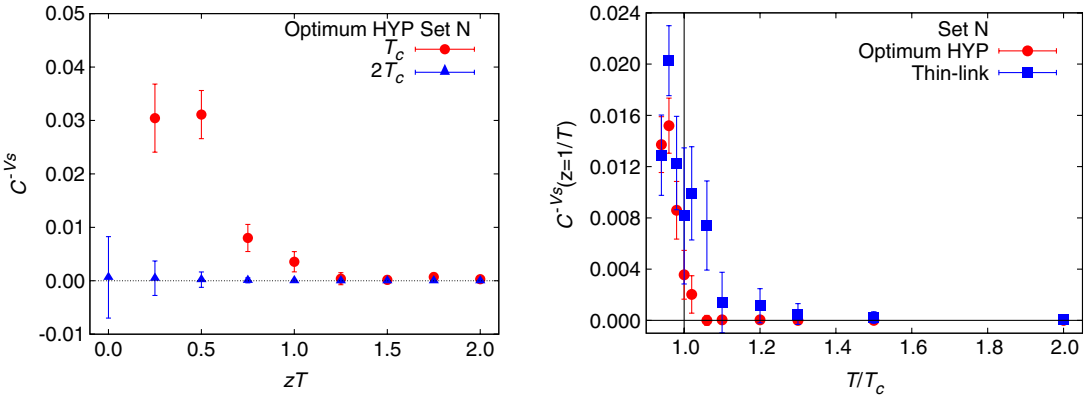

FIG. 5 (color online). The correlator $C^{(-V_s)}$ shows interesting short-distance ($z \leq 1/T$) spatial structure slightly above T_c (left). With smeared correlators the effect barely persists into the hot phase (right). The results are displayed for set N. Sets O and P show similar behavior.

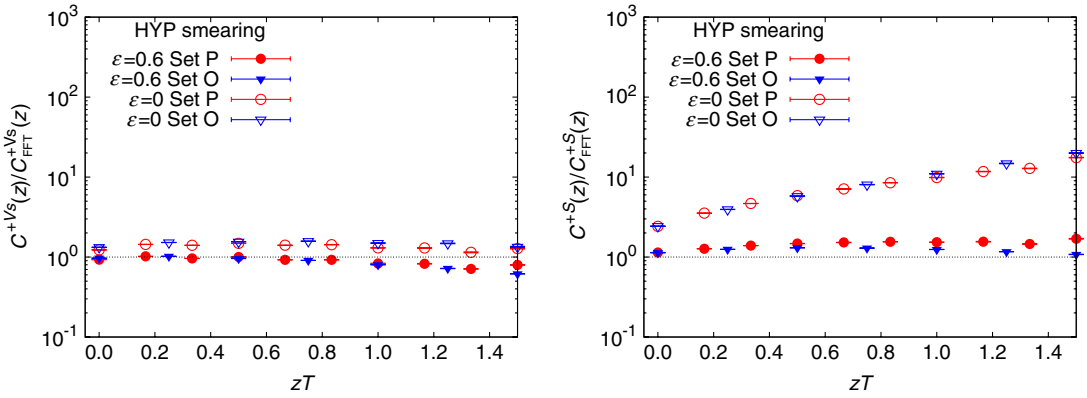

FIG. 6 (color online). The ratio of chiral projections $C^{(+V_s)}$ (left) and $C^{(+S)}$ (right) at $2T_c$ to the respective FFT prediction with data sets O and P. The smeared correlators come close to FFT in both cases, whereas the unsmeared $C^{(+S)}$ is quite different.

temperature dependence is exhibited by showing how $C^{(-V_s)}(z = 1/T)$ changes with T. Below T_c the correlator does not vanish, but the spatial structure seems to have entirely disappeared for $T > 1.05T_c$. With unsmeared correlators the effect persists further into the hot phase. This gives one definition of the width of the chiral crossover; it is larger than the one implied by $\Delta\beta_c$ (see Appendix).

$C^{(+V_s)}$ is close to the FFT prediction with either thin-link or smeared valence quarks. With thin-link staggered valence quarks, we see that $C^{(+S)}$ is different from FFT, as previously observed. However, on smearing, they become compatible with FFT (see Fig. 6). This is a more detailed understanding of why the meson screening correlators are nearly degenerate in Fig. 4.

In Fig. 7 we show that the correlator $C^{(+S)}(z)$ approaches FFT as the parameter ϵ is tuned to the optimum in each of the smearing schemes, approaching closest to FFT at the optimum. We used the distance $z = 1/T$ in this demonstration because it is neither in the far IR nor in the UV. The optimum HYP and HEX schemes bring the correlator closer to FFT than the APE and Stout smearing schemes,

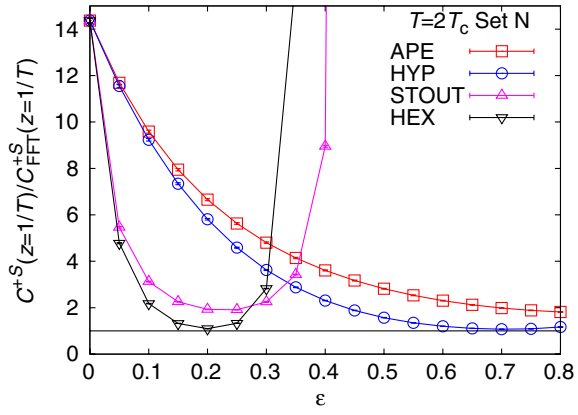

FIG. 7 (color online). The correlator $C^{(+S)}(z = 1/T)$ at $2T_c$ from set N, normalized by its value in FFT, as a function of the smearing parameter ϵ in various smearing schemes.

although the latter also come very close to FFT. Next we explore this difference between schemes.

C. Smearing, taste symmetry and screening masses

On examining screening masses, we found that they depend on the smearing parameter ϵ essentially only through the taste symmetry breaking measure

$$\delta m_\pi = m_{\gamma_5\gamma_i} - m_{\gamma_5}, \tag{6}$$

where the subscripts on the right denote the pion taste structure. The γ_5 taste is the Goldstone pion. We chose the partner with taste structure $\gamma_5\gamma_i$ as an indicator of taste splitting since it turned out to be relatively easily measured. Figure 8 shows the nearly linear dependence of μ/T on $\delta m_\pi a$. The figure shows the clear superiority of the HEX scheme over the Stout. Using the scaling shown in Fig. 8, one could extrapolate screening masses to the limit $\delta m_\pi \to 0$. However, this is premature, since it involves an extrapolation to suboptimal values of ϵ. The S/PS screening masses obtained using local operators with dynamical p4 quarks at a comparable temperature turns out to be around $4.8T$ [6].

More information can be extracted from the taste splitting of the screening masses at finite T,

$$\delta\mu_{\rm PS} = \mu_{\gamma_5\gamma_i} - \mu_{\gamma_5}. \tag{7}$$

The only previous study of this kind was reported in Ref. [6]. In Fig. 8 we show $\delta\mu_{\rm PS}$ as a function of $a\delta m_\pi$. In making this comparison, we held the lattice spacing fixed, with one set of measurements at $T = 0$, one at $T = 2T_c$ in set O, and a third at $T = 1.33T_c$ in set P. We find $\delta\mu_{\rm PS} \propto T(a\delta m_\pi)^2$ over the range of values we obtained. This removes the ambiguity remarked upon in Ref. [6].

One can argue for this on general grounds. A hadron mass, M, can be written as $Ma = f(a\Lambda_{\overline{MS}}, ma, \epsilon)$, where we treat ϵ as a generic label for all the parameters that control smearing. A screening mass, μ, can be written as

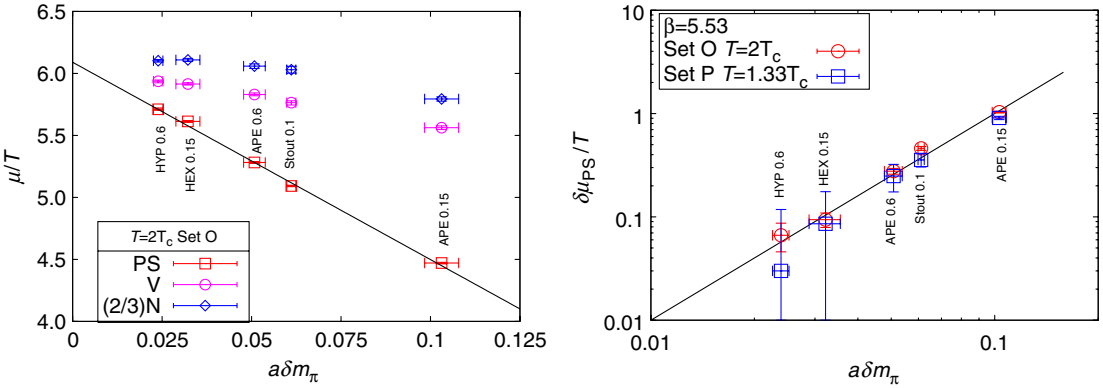

FIG. 8 (color online). The first panel shows screening masses of the local S/PS, V/AV, and N at $2T_c$ as functions of the pion taste splitting $a\delta m_\pi$ at $T = 0$ in data set O. The screening mass of the nucleon has been multiplied by $2/3$ in order to compress the vertical scale. Each set of screening masses varies linearly with a measure of the pion taste splitting, $a\delta m_\pi$. The second panel plots $a\delta m_\pi$ at $T = 0$ against the splitting of the corresponding screening masses, $a\delta\mu_{\rm PS}$ at two different temperatures, but at the same lattice spacing; the line $y = 100x^2$ is superposed to indicate the slope.

$\mu/T = g(a\Lambda_{\overline{MS}}, ma, \epsilon, N_t)$, since $N_t = 1/(aT)$, or as $a\mu = g'(a\Lambda_{\overline{MS}}, ma, \epsilon, N_t)$. For data taken at fixed cutoff, $a\Lambda_{\overline{MS}}$, we need not show this parameter explicitly. Although we work at fixed ma, it is profitable to consider the dependence on this variable. A series expansion in ma near the chiral limit would yield different dependence for the Goldstone pion mass,

$$am_{\gamma_5} = \alpha_1\sqrt{ma} + \mathcal{O}(ma)^{3/2}, \quad \text{and}$$
$$aM = \gamma_0 + \gamma_1 ma + \mathcal{O}(ma)^2, \tag{8}$$

where M is any other mass scale, and the coefficients depend on ϵ. As a result, $a\delta m_\pi = \gamma_0 - \alpha_1\sqrt{ma} + \gamma_1 ma$ and $\delta\mu_{\rm PS}/T = \gamma_0' + \gamma_1' ma$. If taste symmetry were recovered in the chiral limit by tuning ϵ, then one might argue that $\gamma_0 = \gamma_0' = 0$ and hence $a\delta\mu_{\rm PS} \propto (a\delta m_\pi)^2$. This would also mean that all pion tastes are forced to be Goldstones, with an expansion starting at order $\sqrt{ma}$. Chiral logarithms, which we have neglected here, could become important at smaller masses and spoil this scaling.

Even if smearing achieves a more limited goal of significantly decreasing δm_π at finite ma without actually recovering taste symmetry completely, one might still recover quadratic scaling. All that is needed is that γ_0 and γ_0' become much smaller than the actual $T = 0$ taste splitting in the problem. In general, one would have

$$\delta\mu_{\rm PS}/T - \gamma_0' \propto (a\delta m_\pi - \gamma_0)^2. \tag{9}$$

The data in Fig. 8 shows that γ_0' and γ_0 are small compared to $a\delta m_\pi$. This quantifies how well smearing works. The fact that it seems to work better at finite temperature than at $T = 0$ with fixed values of $a\Lambda_{\overline{MS}}$ and ma possibly indicates that the Dirac eigenvalue spectrum is simpler. We shall return to this point later.

The main conclusion from these studies of smearing is the following. Optimizing the suppression of UV modes automatically improves taste symmetry in the hadron spectrum at $T = 0$. This leads to superlinear improvement in taste symmetry in the hot phase of QCD. In order to gain most from such an improvement, one should then choose the best possible smearing scheme. With partial quenching, as here, this would mean working with the optimized HYP scheme; with dynamical smeared quarks, it would mean working with the optimized HEX scheme.

IV. RESULTS

A. Hot QCD: weak coupling and the Dirac spectrum

We found that the mass splitting between chiral partners changes rapidly in the low-temperature phase and vanishes fairly close to T_c in the hot phase. In Fig. 9 we show that Δ_S and Δ_V both vanish at $T = 1.05T_c$. Also, a comparison of sets N and O shows very little quark mass dependence at about the same lattice spacing. These results are in contrast to the observations in Refs. [4,5] that Δ_S remains significantly nonzero up to a temperature significantly higher than T_c. The change from the old results [4] using the same data set P confirms that the improvement is due to smearing.

The rapid approach to behavior similar to the weak-coupling theory has implications for the spectrum of the staggered Dirac operator. The vanishing of the pion mass in the chiral limit at $T = 0$ is related to a finite density of the Dirac eigenvalues near zero. It was shown earlier in a study of set O with thin-link quarks that a gap developed in the massless staggered eigenvalue spectrum a little above T_c and that the hot phase contained localized Dirac eigenvectors [21].

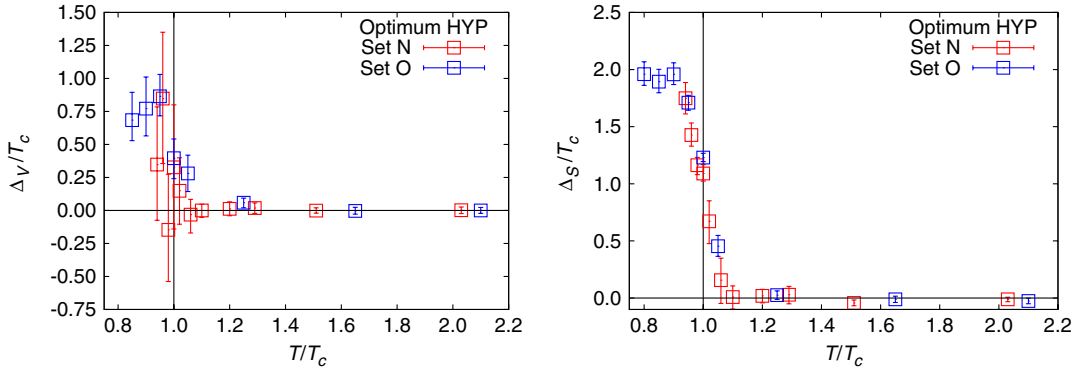

FIG. 9 (color online). Variation of Δ_V (left) and Δ_S (right) with temperature. Δ_V approaches 0 at the 95% confidence level immediately above T_c, independent of smearing scheme and quark mass.

Here we studied the gap by measuring the smallest eigenvalue of the massless staggered Dirac operator, λ_0. The ensemble average, $\langle\lambda_0\rangle$, at a given temperature was generally seen to be within a factor of 4 of the minimum over the ensemble. In view of this, we report $\langle\lambda_0\rangle$. As can be seen in Fig. 10, it climbs by 2 orders of magnitude between T_c and $1.06T_c$ for the smeared Dirac operator. For the thin-link operator, $\langle\lambda_0\rangle$ rises at significantly higher temperature.

One sees some volume dependence in the result. This was studied extensively in Ref. [21], in which it was found that the volume dependence becomes negligible when the spatial size, L, is of the order of $1/\langle\lambda_0\rangle$. For $LT = 4$ this would be at $\langle\lambda_0\rangle \simeq 0.25$, which seems to happen at $1.5T_c$. In the future it would be interesting to study this volume dependence further.

It is also of interest to note that $a\langle\lambda_0\rangle$ becomes comparable to am at $T = T_c$ with optimum HYP smearing. Since this happens for all the data sets, it accounts for the lack of quark mass dependence seen in Δ_V and Δ_S. With thin-link quarks, this crossing is delayed to $T/T_c \simeq 1.5$, thus affecting all screening phenomena.

In set N at $T = 1.3T_c$, we spotted one configuration out of the 50 for which λ_0 was 2 orders of magnitude below $\langle\lambda_0\rangle$. This implies the existence of a small fraction of atypical configurations in the thermal ensemble. These would be interesting in a study of axial U(1) symmetry at finite temperature, in which such atypical configurations have been linked to topological configurations by observations with overlap [22] or highly improved staggered quarks in Ref. [23]. However, that would require a much larger statistical sample and is, therefore, best left to the future.

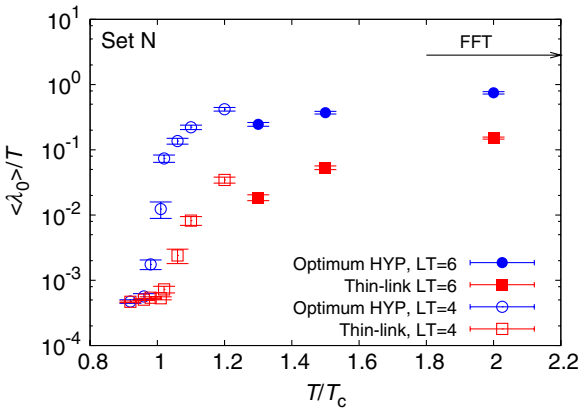

FIG. 10 (color online). The ensemble averaged smallest eigenvalue of the massless staggered Dirac operator, $\langle\lambda_0\rangle$, for set N. With optimal HYP smearing, the eigenvalue rises by two orders of magnitude in a narrow range above T_c. For the thin-link Dirac operator, the rise is much slower.

B. Comparison with weak-coupling theory

Finally, the results for the screening masses as functions of T are shown in Fig. 11 for all three data sets with optimal HYP smearing. Also shown are the values expected in FFT on lattices with the same size. The analysis of correlation functions obtained with these smeared valence quarks shows that the screening masses in all channels approach FFT at high T. The most striking new feature of this data is that this approach is from above, in conformity with the predictions of Ref. [8]. Similar results are obtained with optimal HEX smeared quarks. We have shown earlier in Fig. 8 that there is a remaining uncertainty of around 15% in the determination of the S/PS screening mass. This comes from the residual taste symmetry breaking at the best optimization of the screening parameters possible at this lattice spacing. Reduction of this uncertainty requires going to finer lattices.

The weak-coupling prediction for the mesonlike screening masses is

$$\mu = \mu_{\mathrm{FFT}} + \frac{4}{3}\alpha_S[1 + 2E_0]T. \tag{10}$$

Here α_S is the two-loop QCD coupling evaluated in the $\overline{MS}$ scheme at the scale $2\pi T$. $E_0 = 0.3824$ for two flavors of quarks in a dimensional reduction scheme evaluated in the

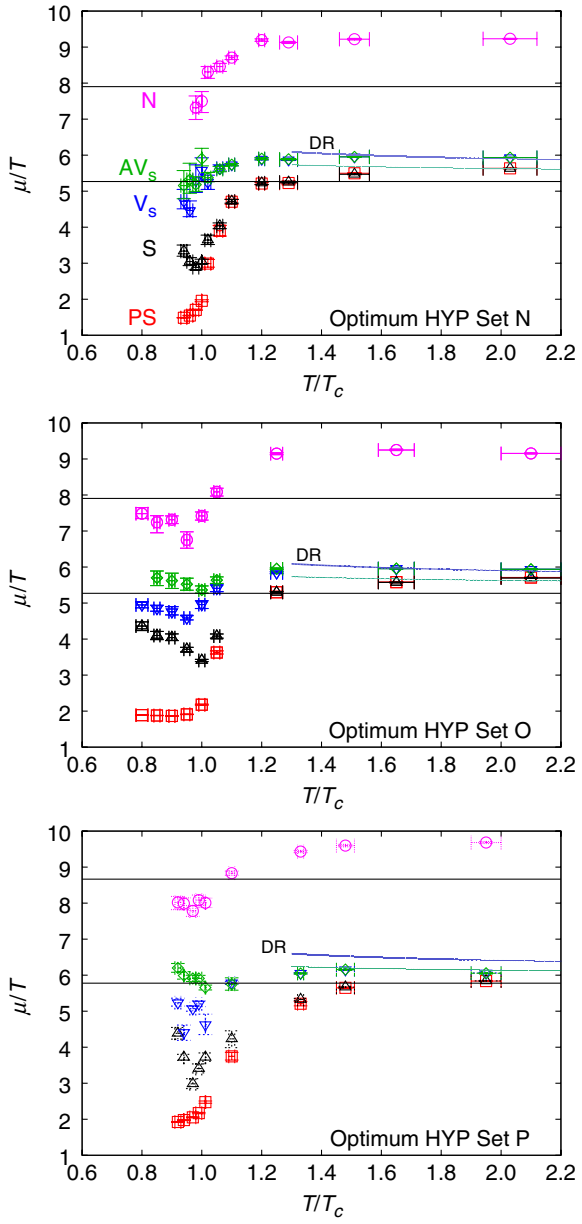

FIG. 11 (color online). Hadron screening masses for the data sets N, O, and P using optimum HYP smeared correlators. The horizontal lines are the free theory screening mass for the nucleon and the mesons, respectively: for sets N and O, they are 5.27 for mesons and 7.90 for baryons; for set P they are 5.78 for mesons and 8.67 for baryons. Dimensional reduction (DR) denotes the weak-coupling prediction of Ref. [8]; the unlabelled line immediately below this shows the prediction of Ref. [9].

continuum [8]. A hard thermal loop resummation that neglects soft gluon contributions to the vertex yields $E_0 = 0$ [9]. These weak-coupling predictions are also shown in Fig. 11, with α_S determined using Ref. [24]; since there is no computation with weak coupling on a lattice, the effect of finite lattice spacing on E_0 cannot be estimated. Nevertheless, as one can see, both the weak-coupling predictions are close to the observed screening masses.

V. CONCLUSIONS

Several properties of quarks at experimentally accessible temperatures above T_c seem to be explained in weak-coupling QCD. However, one that showed puzzling departures from weak-coupling predictions was screening masses from hadronic excitations. In quenched computations it was seen that the results depended strongly on the kind of valence quark used [10]. With this clue in hand, we performed computations with dynamical staggered sea quarks and improved valence quarks in three sets of computations, one new (set N, see Table I) and two older (sets O [16] and P [17]). Studies with staggered valence quarks were reported earlier with set P [4].

A preliminary part of this work was the optimization of the valence quarks. We used four popular versions of fat-link staggered quarks. We optimized the smearing parameter, ϵ, in each case by observing changes to the power spectrum of the plaquette (see Fig. 2) and the largest and smallest eigenvalues of the Dirac operator (see Fig. 3). The optimum ϵ was chosen so that the UV was suppressed as much as possible without changing the IR behavior in both cases. This also improved the performance of the conjugate gradient algorithm used for the inversion of the Dirac operator (see Table II). Such a tuning was done at $T = 0$. We found mild changes in the tuning parameters as the lattice spacing was changed by a factor of 2.

Although the smearing parameter is optimized by requiring that the IR components of fields do not change appreciably, it does affect the long-distance properties of the theory, such as masses. We compared different schemes through a measure of the recovery of staggered quark taste symmetry in the spectrum of pions (see Fig. 8). The optimized HYP smearing works best, although optimized HEX smearing is a close second. This is pleasant since dynamical simulations with HEX smearing are easier than with HYP.

Smearing causes systematic changes in finite temperature properties of interest. We found that the screening mass in the hot phase increases systematically as taste symmetry breaking is reduced at $T = 0$ (see Fig. 8). Also, taste symmetry breaking in the hot phase improves superlinearly with improvement at $T = 0$ (see Fig. 8). Since recovery of taste symmetry has been used as the main indicator of the reduction of UV effects, it is natural in this study to use optimized HYP smearing in order to best reduce lattice artifacts.

On doing this we find that the screening correlator recovers the degeneracies that a theory of weakly coupled fermions would predict (see Fig. 4). This happens very close to, and above, T_c (see Fig. 5). The correlators themselves are also close to the predictions of a free fermion field theory (see Fig. 6). Consistent with this, the screening

masses at high temperature are found to be close to the weak-coupling theory (see Fig. 11). A computation in dimensional reduction [8] gives results that are slightly different from a hard thermal loop computation neglecting soft-gluon effects on the vertex [9]. The lattice computation is unable to distinguish these as yet, but we may expect this to improve in the near future.

We also see that the smallest eigenvalue of the optimally HYP smeared massless staggered Dirac operator shows a rapid jump from extremely small values in the mean below T_c to fairly large values above (see Fig. 10). The behavior of the thin-link staggered operator is qualitatively similar, although quantitatively slower to change. Since the smallest eigenvalue of the massless smeared operator is comparable to the bare mass already at $T = T_c$, the limit of physical renormalized mass becomes easy to take in the high-temperature phase. There is evidence for a very small fraction of completely atypical configurations in the hot phase. A study of the topology of these gauge configurations lies outside the scope of this paper.

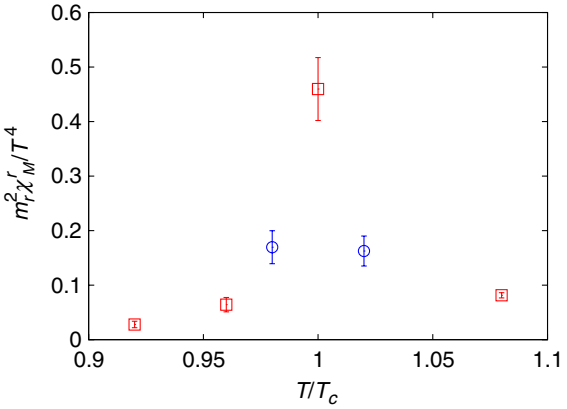

FIG. 12 (color online). Dependence of $m_r^2\chi_M^r/T^4$ on T/T_c. The data points marked by boxes are measurements made on the line of constant m/T_c, whereas those marked by circles are obtained with constant am.

ACKNOWLEDGMENTS

The lattice computations described here were performed on the Cray X1 of the Indian Lattice Gauge Theory Initiative in TIFR. We thank Ajay Salve and Kapil Ghadiali for technical assistance. We also thank Debasish Banerjee, Saumen Datta, Mikko Laine, Nilmani Mathur, Subroto Pal, and Christian Schmidt for their comments. Some of the configurations used in this study were generated earlier for other studies by the ILGTI.

APPENDIX: DETERMINATION OF β_c

The crossover is determined at $N_t = 4$ for a bare quark mass $a_c m = 0.015$, where a_c is the lattice spacing at β_c. We determined β_c by positions of the peaks of different susceptibilities. $\Delta\beta_c$ was defined to be the full width at half maximum of the same susceptibilities.

We measured the Wilson line susceptibility, χ_L [17], the bare chiral susceptibility, χ_M [25], the corresponding renormalized quantity $m_r^2\chi_M^r/T^4$ [26], and the fourth-order quark number susceptibilities, χ_{22} and χ_{40} [16], at various values of β in the crossover region. For the measurement of $m_r^2\chi_M^r/T^4$, we determined the chiral condensate at zero temperature on 16^4 lattice at the same values of β as the finite temperature ones.

Prior to the runs listed in Table I, we performed a series of runs at fixed bare quark mass, $am = 0.015$, with $N_s = 8$ and 12. We used these runs to make first estimates of β_c and followed up with the runs along lines of constant m/T_c listed in Table I. The compatibility of these runs is shown in Fig. 12, where $m_r^2\chi_M^r/T^4$ is given as a function of T/T_c. The figure also shows that with this cutoff, the deconfining and chiral crossovers in QCD coincide; $m_r^2\chi_M^r/T^4$ peaks between 0.98 and $1.02T_c$.

To determine β_c accurately, we interpolated data for susceptibilities using multihistogram reweighting [27] in the crossover region. From bootstrap resampling of the histograms, we determined the means and errors in the position of the peak of each susceptibility and its full width

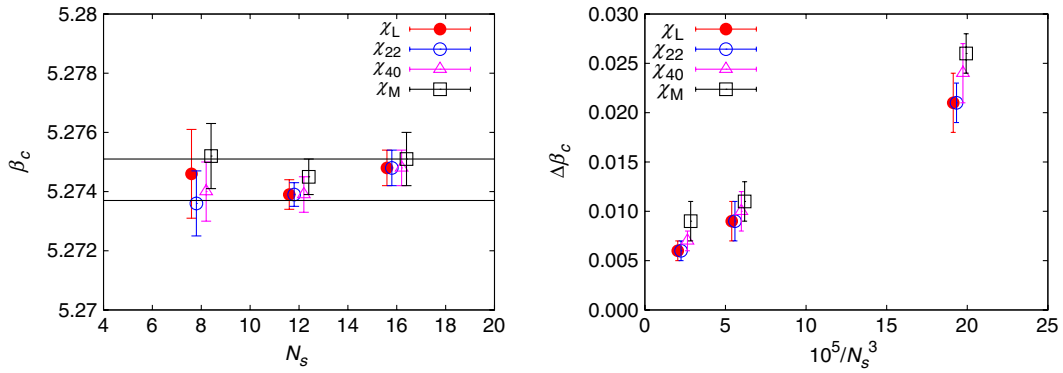

FIG. 13 (color online). The spatial size dependence of β_c (left) and $\Delta\beta_c$ (right). The lines enclose 68% confidence limits on β_c, obtained by fitting a single constant to all the estimates. Points at equal N_s are horizontally displaced for visibility.

TABLE III. β_c and $\Delta\beta_c$ as determined from different susceptibilities. $\Delta\beta_c$ is much larger than the statistical error in β_c.

	β_c	$\Delta\beta_c$
χ_M	5.2747(6)	0.009(2)
χ_L	5.2743(5)	0.006(1)
χ_{22}	5.2741(5)	0.006(1)
χ_{40}	5.2743(6)	0.007(1)

at half maximum, so obtaining β_c and $\Delta\beta_c$ [28]. We found β_c and $\Delta\beta_c$ for each of the susceptibilities on the three different lattice volumes, the results of which are shown in Fig. 13. Since we found very little volume dependence in β_c, we made a fit to a constant, independent of volume. The values of β_c so determined are displayed in Table III. In Fig. 13 we also show the volume dependence of $\Delta\beta_c$. This decreases with the volume and gives some indication of saturating, within errors, close to our largest lattice. Therefore, we take $\Delta\beta_c$ obtained on $N_s = 16$ as our best estimate. These estimates are also listed in Table III. We find that the variation in β_c with different susceptibilities occurs well within the width of the crossover measured from each indicator separately. In fact, the four estimates of β_c are consistent with each other within 68% confidence limits. Combining all four measurements, we quote $\beta_c = 5.2744(7)$ and $\Delta\beta_c \approx 0.006$.

[1] J. P. Blaizot, E. Iancu, and A. Rebhan, Phys. Lett. B **523**, 143 (2001); A. Vuorinen, Phys. Rev. D **67**, 074032 (2003); Y. Schroder and M. Laine, arXiv:hep-lat/0509104.
[2] C. E. Detar and J. B. Kogut, Phys. Rev. Lett. **59**, 399 (1987).
[3] K. D. Born, S. Gupta, A. Irbäck, F. Karsch, E. Laermann, B. Petersson, and H. Satz, Phys. Rev. Lett. **67**, 302 (1991).
[4] D. Banerjee, R. V. Gavai, and S. Gupta, Phys. Rev. D **83**, 074510 (2011).
[5] M. Cheng *et al.*, Eur. Phys. J. C **71**, 1564 (2011).
[6] E. Laermann and F. Pucci, Eur. Phys. J. C **72**, 2200 (2012).
[7] B. B. Brandt *et al.*, Proc. Sci., LATTICE2012 (2012) 073.
[8] M. Laine and M. Vepsäläinen, J. High Energy Phys. 02 (2004) 004.
[9] W. M. Alberico, A. Beraudo, A. Czerska, P. Czerski, and A. Molinari, Nucl. Phys. **A792**, 152 (2007).
[10] S. Datta, S. Gupta, M. Padmanath, J. Maiti, and N. Mathur, J. High Energy Phys. 02 (2013) 145.
[11] M. Albanese *et al.*, Phys. Lett. B **192**, 163 (1987).
[12] A. Hasenfratz and F. Knechtli, Phys. Rev. D **64**, 034504 (2001).
[13] C. Morningstar and M. J. Peardon, Phys. Rev. D **69**, 054501 (2004).
[14] S. Capitani, S. Dürr, and C. Hoelbling, J. High Energy Phys. 11 (2006) 028.
[15] K. Orginos, D. Toussaint, and R. L. Sugar, Phys. Rev. D **60**, 054503 (1999); E. Follana, C. Davies, A. Hart, P. Lepage, Q. Masonv, and H. Trottier, Nucl. Phys. B, Proc. Suppl. **129–130**, 384 (2004); T. Bae, D. Adams, C. Jung, H.-J. Kim, J. Kim, K. Kim, W. Lee, and S. Sharpe, Phys. Rev. D **77**, 094508 (2008).
[16] R. V. Gavai and S. Gupta, Phys. Rev. D **71**, 114014 (2005).
[17] R. V. Gavai and S. Gupta, Phys. Rev. D **78**, 114503 (2008).
[18] G. H. Golub and C. F. van Loan, *Matrix Computations* (Johns Hopkins University Press, Baltimore, 1996).
[19] M. F. L. Golterman, Nucl. Phys. **B273**, 663 (1986).
[20] T. Kurth *et al.*, Proc. Sci., LATTICE2010 (2010) 232.
[21] R. V. Gavai, S. Gupta, and R. Lacaze, Phys. Rev. D **77**, 114506 (2008).
[22] R. V. Gavai, S. Gupta, and R. Lacaze, Phys. Rev. D **65**, 094504 (2002).
[23] H. Ohno *et al.*, Proc. Sci., LATTICE2012 (2012) 095.
[24] S. Gupta, Phys. Rev. D **64**, 034507 (2001).
[25] E. Laermann, Nucl. Phys. B, Proc. Suppl. **63**, 114 (1998).
[26] Y. Aoki, Z. Fodor, S. D. Katz, and K. K. Szabó, Phys. Lett. B **643**, 46 (2006).
[27] A. M. Ferrenberg and R. H. Swendsen, Phys. Rev. Lett. **63**, 1195 (1989).
[28] S. Datta and S. Gupta, Phys. Rev. D **80**, 114504 (2009).